Radiative Effects of Increased Water Vapor Associated with Enhanced Dustiness in the Saharan Air Layer

C.L. Ryder[1]

[1]Department of Meteorology, University of Reading, Reading, RG6 6BB, UK.

Corresponding author: Claire Ryder (c.l.ryder@reading.ac.uk)

Key Points:

- Observations show enhanced moisture in the upper Saharan Air Layer (SAL) associated with dust, counter to the conventional dry layer model
- Enhanced moisture reduces the magnitude of the negative direct radiative effect from dust at the top of atmosphere by 11%
- Observed water vapor structure leads to enhanced cooling in the moist upper-SAL and heating in the dry lower-SAL under dustier conditions

Abstract

The Saharan Air Layer (SAL) has been shown to be an elevated, well-mixed, warm, dry, frequently dusty layer. The structure of the SAL plays an important role in regional climate and in long-range dust transport. A new analysis of aircraft observations shows that although increased dustiness in the SAL is associated with drier conditions in the lower-SAL as expected, dustiness is also associated with increased moisture in the upper-SAL. We assess the radiative effects of the observed dust and increased water vapor (WV) using a radiative transfer model.

The observed WV in the upper-SAL affects the top-of-atmosphere (TOA) direct radiative effect (DRE), while lower-SAL WV affects the surface DRE and column atmospheric heating. TOA DRE is negative for dust-only, while including both the observed dust and WV reduces the magnitude of the negative TOA DRE by 11%. The observed WV structure increases the negative surface DRE from dust by 8% and increases atmospheric heating by 17%. These effects are driven by longwave (LW) radiation, whereby WV changes increase the positive TOA LW DRE by 30%, decrease the surface LW DRE by 52% and change the sign of LW atmospheric heating from negative to positive. The observed WV profile leads to enhanced cooling in the moist upper-SAL and heating in the dry lower-SAL under dustier conditions. Increased WV in the SAL is consistent with other studies demonstrating a trend of increased WV over the Sahara. This work demonstrates the importance of the upper-SAL WV profile in determining the radiative effect dust.

Plain Language Summary

During summer, warm, dry, dusty air is transported from the Sahara across the Atlantic Ocean in an elevated plume. This plume has many impacts on climate, such as suppressing convection which may be important to hurricane development, and transporting dust particles which can supply nutrients to the oceans and degrade respiratory health. Previously the plume has been found to be very dry, but by using new observations from a research aircraft, we show that high

levels of moisture are found at its top. This is important because it alters the balance of heating and cooling at different altitudes within the atmosphere, which has not been accounted for in this way before, and may impact how Saharan air interacts with weather in the Atlantic region and how easily dust is transported over long distances. We find that the addition of moisture at the top of the plume adds a warming of 11% compared to the effects from dusty air, and decreases in moisture at lower altitudes can change the nighttime effect of the plume from cooling to heating. Therefore future work should take into account the vertical distribution moisture in Saharan dust plumes as well as the dust itself.

1 Introduction

The Saharan Air Layer (SAL) is conventionally considered to be a deep warm, dry, elevated layer of air which exists over the tropical north Atlantic Ocean from late spring to early fall, frequently containing mineral dust transported from North Africa (Braun, 2010). The SAL originates from strong surface heating over the Sahara desert, where a deep, well-mixed, warm, dry boundary layer develops, typically extending up to 5 to 6 km, known as the Saharan Boundary Layer (Engelstaedter et al., 2015; Marsham et al., 2013). The SAL, and any embedded mineral dust, is transported westwards by prevailing winds and steered by African Easterly Waves. As it moves over the Atlantic Ocean, it is undercut by a moist marine boundary layer (MBL), forming an elevated mixed layer known as the SAL, characterized by near-constant potential temperatures and water vapor (WV) mixing ratios, and retaining its structure as it is transported westwards (Carlson, 2016; Dunion & Velden, 2004).

In the original conceptual model of the SAL (e.g. (Carlson & Prospero, 1972; Dunion, 2011; Karyampudi et al., 1999; Prospero & Carlson, 1972) the SAL is shown to be warm, dry and to varying degrees, dust laden. For example, reported values of WV mixing ratios within the eastern SAL are around 2 to 5 g/kg (Carlson & Benjamin, 1980; Carlson & Prospero, 1972; Ismail et al., 2010; Karyampudi et al., 1999), and 1 to 6 g/kg in the western SAL (Dunion, 2011; Dunion & Velden, 2004). Kanitz et al. (2014) present measurements across the width of the tropical Atlantic, finding WV mixing ratios between 3 to 7 g/kg within the SAL. Warm, dry anomalies in the SAL between 800 to 900 hPa have been shown to be related to increased dust optical depth. Together the dusty, dry anomalies are responsible for heating the lower SAL and maintaining the temperature inversion its base, as well has playing a role in suppressing deep convection and increasing low cloud fraction (Doherty & Evan, 2014; Wong & Dessler, 2005; Wong et al., 2009).

Around 50% of dust events in the summertime Sahara are driven by cold pool outflows (haboobs), with the dust being associated with elevated moisture levels deriving from moist downdrafts (Marsham et al., 2013; Marsham et al., 2008). Several studies have described the role of cold pool outflows and density currents in transporting dust and moisture into the arid Sahara (Allen et al., 2013; Engelstaedter et al., 2015; Flamant et al., 2007). Marsham et al. (2016) examined the relative radiative effects of dust and WV in the Saharan heat low (SHL), finding that WV variations exert a dominant role on the top of atmosphere (TOA) radiation budget, while dust variability was dominant in driving atmospheric heating and surface radiation. Gutleben et al. (2019) found that SAL WV mixing ratios over the western Atlantic for one dust event were elevated compared to those in the surrounding free atmosphere, and found that the altered WV profile within the dust led to substantial changes in radiative heating rates.

Here we examine dust and WV aircraft observations in the tropical north Atlantic Ocean region. During research flights, it was noticed that specific humidity often increased when dust layers were penetrated, and was particularly noticeable during a few extremely large dust events (Marenco et al., 2018). Since this increased moisture within the dusty SAL is counter to the conventional model of a dry, dusty SAL, here we examine the evidence from airborne observations and evaluate the radiative effect of the observed changes in dust and enhanced water vapor.

2 Methods

2.1 Aircraft Observations

We present meteorological and aerosol in-situ aircraft observations from the AERosol Properties – Dust (AER-D) airborne field campaign (Marenco et al., 2018) which took place during August 2015 in the region of the Cape Verde Islands (Figure 1). The Facility for Atmospheric Airborne Measurements BAe146 research aircraft sampled a series of dust events in the SAL between 7 and 25 August 2015, described in more detail by Ryder et al. (2018), Liu et al. (2018), Marenco et al. (2018), where microphysical, chemical, optical and radiative properties of the dust samples are presented.

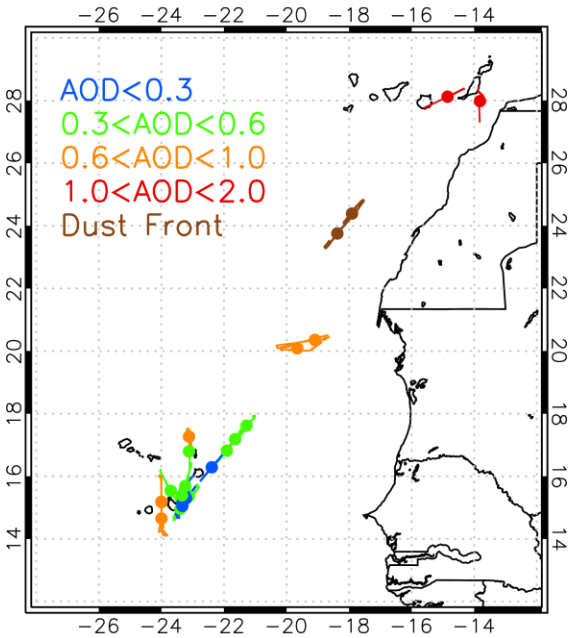

Figure 1: Locations of AER-D aircraft profiles analysed in this study. Lines show locations sampled during profile ascents or descents, solid dots indicate mean profile location. Colors indicate AOD as shown in the legend.

Here we use in-situ observations from 24 aircraft profile descents and ascents as shown in Figure 1, sampled during 6 flights (also shown in Ryder et al. (2018), their table 2). Profiles cover altitudes from close to the ocean surface to above the SAL, generally ~5.5 km. All the dust

events sampled during AER-D were driven by outflows from mesoscale convective systems ('haboobs,' identified in Ryder et al. (2018), which in most cases were mixed vertically throughout the Saharan boundary layer by convective mixing before being advected over the ocean in an elevated SAL. However, two flights (b923, b924) sampled a large dust plume with aerosol optical depths (AODs) at 550 nm greater than 1, further to the north close to the Canary Islands. Two particular profiles sampled an extremely unusual dust structure with very high dust concentrations peaking at low altitudes of around 1 km, constituting a clear 'dust front' which kept its structure (low altitude, intense dust concentrations) while being advected out over the Atlantic Ocean (brown lines in Figure 1). This event is investigated in more detail by Marenco et al. (2018), and is referred to here as the 'dust front' case since it is different to the other, more typical elevated dust profiles sampled.

Airborne measurements of temperature are taken from a Rosemount/Goodrich type 102 Total Air Temperature probe, using the non-deiced models for all flights except b934 when data is not available, and when the deiced model was used instead. Dew point temperature measurements, used to calculate water vapor mixing ratios are taken from the Sky Phys Tech Inc. Nevzorov total water content probe (Korolev et al., 1998), except for flights b923, b934 and b932 Profile 1 where they are taken from the General Eastern 1011B Chilled Mirror Hygrometer. Pressure was measured by a reduced vertical separation minimum data system.

Ryder et al. (2018) have shown that the aerosol load sampled was predominantly mineral dust, including the aerosol in the marine boundary layer. Here we take a straightforward indication of dust loading from the dust extinction at 550 nm, calculated by summing dust scattering and absorption. Scattering is measured by a TSI 3563 integrating nephelometer (550 nm wavelength used here) and absorption measurements were made by a Radiance Research particle soot absorption photometer (PSAP) at 567 nm. Further details and processing information can be found in Ryder et al. (2018). Extinction is integrated vertically from aircraft profiles to provide AODs at 550 nm.

2.2 Radiative Transfer Calculations

We employ the Suite Of Community RAdiative Transfer codes based on Edwards and Slingo (SOCRATES, Edwards and Slingo (1996), Manners et al. (2017)) radiative transfer model (RTM) in order to calculate radiative fluxes. SOCRATES is the RTM implemented by the family of UK Met Office numerical weather prediction and climate models. Here we use the spectral setup analogous to that from HadGEM3 model Global Atmosphere 6 configuration (Walters et al., 2011). A two stream practical improved flux method is used (Zdunkowski et al., 1980).

Shortwave fluxes are calculated over 6 spectral bands from 0.2 to 10 μm and longwave fluxes are calculated in 9 spectral bands from 3.3 to 100 μm. Gaseous absorption is represented according to Cusack et al. (1999) using a correlated-k method. Water vapor terms are based on the HITRAN 2001 database (Rothman et al., 2003) for gaseous absorption coefficients, with updates up to 2003. The water vapor continuum is represented using version 2.4 of the CKD model. Top of atmosphere incoming solar radiation is set to 1365 Wm^{-2}.

SOCRATES requires aerosol vertical profiles in terms of mass mixing ratios. These are calculated to represent dust from the measured in-situ aerosol extinction profiles, converted to a

158 mass loading by using a field campaign specific mass extinction coefficient of 0.36 m^2g^{-1} (Ryder
159 et al., 2018). This value represents the full size distribution up to 100 μm diameter.
160
161 We use 122 vertical levels in SOCRATES, covering 1007 to 0.0005 hPa, with resolution ~20
162 hPa in the lower atmosphere, including the SAL. Observations of dust mass mixing ratio, water
163 vapor mixing ratio and temperature are regridded to the required vertical grid. Only dust aerosols
164 are included. At altitudes above where aircraft data were measured, dust concentrations are set to
165 zero and temperature and water vapor values are set to revert to values from a tropical standard
166 profile (Anderson et al., 1986). Ozone, methane, carbon monoxide, carbon dioxide, nitrous oxide
167 and oxygen profiles are taken from Randles et al. (2012). Shortwave surface albedo is set to 0.05
168 representative of an ocean surface and LW surface emissivity to 0.982 in all spectral intervals.
169
170 Dust optical properties are calculated spectrally in the longwave (LW) and shortwave (SW)
171 spectra using lognormal size distribution parameters representing the AER-D SAL average, as
172 given in Ryder et al. (2018). In the SW, complex refractive index data are taken from Colarco et
173 al. (2014) and LW values from Volz (1973) since these datasets fall centrally in the range from
174 literature (Ryder et al., 2019) and cover the full spectral range required. Mie scattering code (and
175 therefore a spherical particle assumption) is used to calculate spectral optical properties of mass
176 extinction coefficient, single scattering albedo (SSA) and asymmetry parameter, which are
177 applied in SOCRATES and are shown in Table 1. The SSA at visible wavelengths is 0.86,
178 considerably lower than the AER-D campaign mean value of 0.95 at 550 nm (Ryder et al., 2018).
179 The difference occurs due to the spectral averaging applied here which incorporates absorption
180 increasing significantly towards smaller solar wavelengths, as well as the use of the Colarco et
181 al. (2014) imaginary refractive index of 0.0024 at 550 nm compared to a value of 0.0010 derived
182 in Ryder et al. (2018). SOCRATES includes both absorption and scattering in the LW spectrum.
183

Spectral Range	Lower wavelength, μm	Upper wavelength, μm	MEC/m^2g^{-1}	SSA	Asymmetry Parameter
SW	0.20	0.32	0.36	0.70	0.83
	0.32	0.69	0.36	0.86	0.76
	0.69	1.19	0.36	0.95	0.71
	1.19	2.38	0.35	0.93	0.69
	2.38	10.00	0.26	0.82	0.71
LW	25.0	10000.0	0.05	0.28	0.29
	18.2	25.0	0.15	0.36	0.32
	12.5	18.2	0.13	0.42	0.52
	13.3	16.9	0.10	0.37	0.54
	8.3	12.5	0.17	0.42	0.56
	8.9	10.1	0.28	0.45	0.46
	7.5	8.3	0.09	0.41	0.74
	6.7	7.5	0.16	0.62	0.72
	3.3	6.7	0.24	0.87	0.68

184 **Table 1:** Optical properties applied in SOCRATES for each spectral band estimated using
185 refractive index data from Colarco et al. (2014) for the SW, Volz et al. (1973) for the LW and the
186 AER-D mean size distribution (Ryder et al., 2018).

Sensitivity tests have also been carried out using more and less absorbing dust at solar wavelengths. These were calculated using the more absorbing OPAC dataset refractive indices with the OPAC transported mineral dust size distribution (Hess et al., 1998), and the less absorbing refractive index dataset of Balkanski et al. (2007) combined with a smaller dust size distribution (Dubovik et al., 2002). At infrared wavelengths, sensitivity to dust is tested by varying the dust size distribution to the smaller one of Dubovik et al. (2002) and the refractive index to that from OPAC. These calculations yield SSA values of 0.74 and 0.94 for the more and less absorbing cases respectively for the spectral band spanning wavelengths of 0.32 to 0.69 microns.

Surface temperatures for the LW calculations are set based on values observed from aircraft in-situ observations or dropsondes. SW diurnal averages are calculated by running SOCRATES at three solar zenith angles based on the location and time of year of observations, which are multiplied by a gaussian weight and summed.

For each of 24 profiles, 4 radiative transfer simulations are conducted, as outlined in Table 2, in order to isolate the effects of the altered WV profile in the SAL, the presence of dust, and their combined effect. The temperature profile is always taken from aircraft measurements. For the CONTROL, no radiative effects of dust are included. In order to create a WV profile representative of background conditions for the region for the control, a median of the aircraft WV profiles where AOD is less than 0.3 is taken (blue lines in fig 1e and 2a), which represents a non-SAL background WV profile. We do not use the tropical standard WV profile (Anderson et al., 1986), because the non-SAL atmosphere in the region is significantly moister than this (see Figure 1e). The three perturbation experiments shown in Table 2 allow the quantification of the radiative impacts relative to a typical background, non-dusty state in the region. For the dust only experiment (DU), dust observations from aircraft measurements are included, but the background WV profile maintained, such that only the radiative impact of dust is assessed. For the water vapor only experiment (WV), no dust is included, but the water vapor profile used is taken from the aircraft observations. Finally, for DU+WV, both the aircraft-observed dust and water vapor profiles are included to assess their combined effect. For each experiment, vertical profiles of SW and LW radiative fluxes and heating rates are calculated for all aircraft profiles.

Experiment Name	**Abbreviation**	**Temperature Profile**	**Dust Profile**	**Water Vapor Profile**
Control	CONTROL	Aircraft observations	None	Background WV profile: median of WV profiles where AOD<0.3
Dust only	DU	Aircraft observations	Aircraft observations	Background WV profile: median of WV profiles where AOD<0.3
Water vapor only	WV	Aircraft observations	None	Aircraft observations
Dust and water vapor	DU+WV	Aircraft observations	Aircraft observations	Aircraft observations

Table 2: SOCRATES experiments. Each experiment is performed for each of 24 aircraft profiles.

The direct radiative effect (DRE) due to each experiment relative to the control is calculated as defined in equation 1.

$$DRE_{lev}^{spect} = NET\_EXPT_{lev}^{spect} - NET\_CONTROL_{lev}^{spect}$$

Equation 1

NET refers to the net (downwards minus upwards) radiative flux at a level (lev) either at the top of atmosphere (TOA) or surface (SFC), for spect which can be either the SW spectrum, LW spectrum, or total (SW+LW). EXPT refers to the experiment in question, either DU, WV or DU+WV. DREs calculated are instantaneous, diurnally averaged calculations. Positive values at the TOA indicate a warming of the earth atmosphere system. The atmospheric (ATM) radiative effect, also sometimes referred to as atmospheric radiative convergence and indicating atmospheric column heating when positive, is calculated from $DRE_{ATM}^{spect} = DRE_{TOA}^{spect} - DRE_{SFC}^{spect}$.

3 Results

3.1 Aircraft observations of dust and water vapor

Figure 2 shows the profiles of aerosol extinction and water vapor observed by the aircraft. Each is subset by the measured AOD, selected so that each range contains a reasonable number of profiles. The dust load is clearly be seen to increase as AOD increases, and the expected vertical profile of the SAL develops, with (mostly) enhanced dust centered around 700 hPa.

Water vapor profiles are also shown. It is evident that even in cases without much dust (AOD<0.3, blue), the atmosphere is moister than the tropical standard. This is perhaps not surprising given the large amount of variability across tropical regions for which the tropical standard atmosphere represents (e.g. Dunion (2011)).

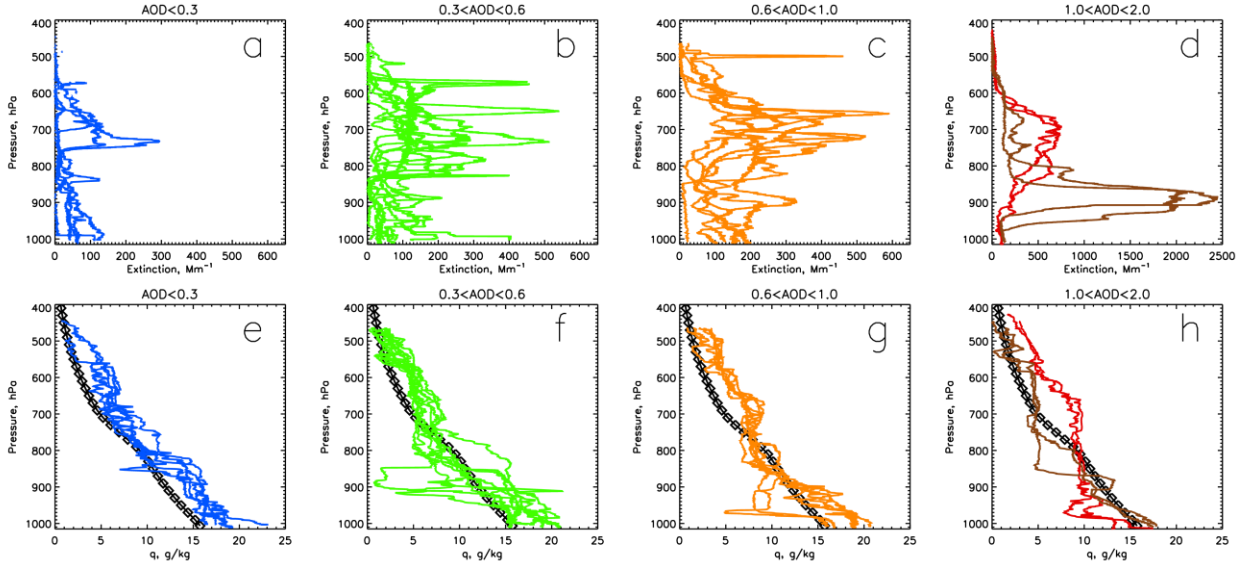

Figure 2. Aircraft profile observations of aerosol extinction (top row) and water vapor mixing ratio (bottom row). Each variable is subset by measured AOD: blue (AOD<0.3, 5 profiles), green (0.3<AOD<0.6, 9 profiles), orange (0.6<AOD<1.0, 6 profiles) and red (AOD>1.0, 4 profiles). Brown lines indicate dust front event. Note that panel (d) extinction x-axis is nearly 5 times as large as (a)-(c). Black diamonds indicate the tropical standard profile. WV profiles shown in panel e are used to create the background WV profile as in Table 2 for the CONTROL experiment.

As AOD increases, the encroachment of the SAL is evident with a deepening of the elevated, well-mixed layer. This can also be seen in Figure 3 where medians for each AOD category, and anomalies relative to the background state are shown. As AOD increases, a well-mixed layer of near-constant potential temperature and water vapor develop, as expected. The well-mixed nature of the SAL means that at lower altitudes, the SAL is warmer and drier than the background state, whereas towards the top of the SAL the atmosphere is cooler and moister than the background state.

Figure 3b clearly shows that under increased AODs (or dust loading), enhanced WV in the upper-SAL and decreased WV in the lower-SAL is observed. This becomes more pronounced as the AOD increases. For AODs over 0.6, enhanced WV is observed for heights above 750 hPa, with anomalies exceeding 2 g/kg for the 1<AOD<2 category (red line). An interesting double-peaked water vapor anomaly structure is seen, whereby anomalies peak at a lower level of around 700 hPa, coincident with the center of the SAL and the anomalies it brings, but anomalies also peak at around 500 hPa, due to the dustier SAL cases extending deeper vertically with more moisture at higher altitudes.

Dust extinction (Figure 3e) and potential temperature (Figure 3c) as a function AOD are also shown, and show the well-mixed and relatively warmer structure of the SAL becoming more clearly defined as it becomes dustier, as expected. It is also notable that the highest AOD category (red) shows a cold anomaly in the upper SAL, at heights above 520 hPa.

The case of the dust front, shown in brown in Figures 2 and 3, is particularly interesting. The extremely high dust loadings are reflected by extinction values of up to nearly 2500 Mm^{-1}, peaking at around 900 hPa (~1km), unusually low altitudes for a dust event over the tropical north Atlantic during summer. The figures show that the peak in dust loadings at ~900 hPa are coincident with an increase in WV content (Figure 2h) up to around 13 g/kg relative to the more well-mixed layer above this with WV mixing ratios of around 5 g/kg. Ryder et al. (2018) and Marenco et al. (2018) have identified this dust event as being an intense haboob which propagated out over the Atlantic at low altitudes, rather than being mixed vertically through the Saharan boundary layer first, as usually occurs. Thus the intense concentration of high moisture and dust loadings at low altitudes can be traced back to cold-pool outflow driving the dust uplift in the form of a recent haboob.

Figure 3f shows the relationship between AOD and precipitable water vapor (PWV) for the whole column (black), for the lower SAL (PWV_lower, p>820 hPa, red), and for the upper SAL (PWV_upper, pressure from 780 to 480 hPa, orange). Overall, as AOD increases, PWV decreases, though there is a large amount of variability and the linear fit has a low correlation (0.18). More insight is gained into the impact of increased dust through viewing the SAL lower

and upper WV changes separately. Figure 3f shows that as AOD increases, PWV_upper increases by 3.8 mm per unit AOD, while PWV_lower decreases by 6.7 mm per unit AOD, with the linear fits showing correlations of 0.58 and 0.59 respectively. For the upper-SAL, PWV_upper increases from 18 mm to 23 mm between the AOD categories of AOD<0.3 and 1<AOD<2 respectively for the profiles shown in Figure 2a (blue vs red). Therefore there is a clear relationship between increased dust load (AOD), decreased lower-SAL moisture, and increased upper-SAL moisture.

Note that the two highest AOD data points (relating to the dust front case) can be viewed to some extent as outliers and are not included in the linear fits. As Figure 3f shows, the two in-situ aircraft profiles sampling this dust front feature demonstrate low PWV_upper and high PWV_lower values, different to the trend demonstrated by the more conventional elevated SAL structure of the other profiles.

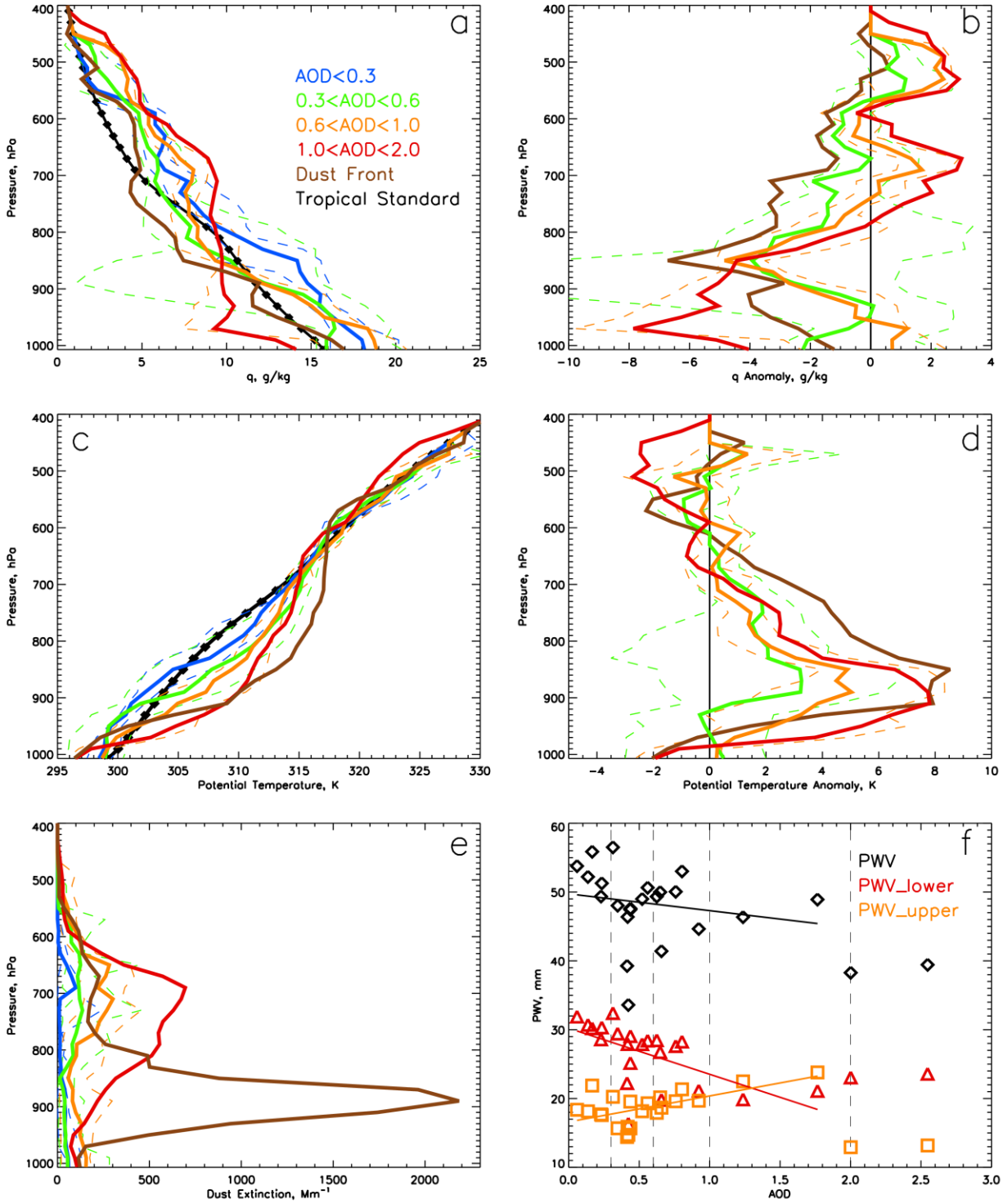

Figure 3. Aircraft observations of (a) water vapor mixing ratio, (c) potential temperature and (e) aerosol extinction; anomalies of (b) water vapor mixing ratio and (d) potential temperature relative to the background state (profiles where AOD<0.3). Profiles are regridded vertically as applied in the RTM. Profiles are grouped by AOD range as indicated with bold lines indicating the median and dashed lines the 10^{th} and 90^{th} percentile ranges for AOD categories where AOD<1. 1<AOD<2 and dust front categories (red and brown) are represented by means as

categories contain only 2 profiles. Black line with symbols indicates tropical standard profile. (f) Relationship for all individual profiles between AOD and PWV, PWV_lower (pressure >820 hPa) and PWV_upper (480 hPa < pressure < 780 hPa), and linear fits where AOD< 2, with Pearson's correlation coefficients of 0.18, 0.58 and 0.59, and dPWV/dAOD values of -2.4, -6.7 and +3.8 mm/AOD respectively**.**

Although the structure of the SAL has been extensively examined and documented, some of the changes found here are not consistent with the conventional view of the SAL's structure. Figures 2 and 3 show much moister values than those documented in most cases, up to 11 g/kg depending on altitude, and with a clear upper SAL moistening with increasing dustiness relative to less dusty cases. Previously, the radiative roles of dust and *dry* SAL air have been assessed (e.g. Wong et al., 2009). Next, we evaluate the radiative effects of the measured dust, and *moist* upper SAL air shown in the observations.

3.2 Impact of altered WV structure on Radiative Effect

Having demonstrated that increased dust loadings were associated with increased upper-SAL WV (PWV_upper) but decreased lower-SAL WV (PWV_lower) during AER-D, the DREs from dust only, WV only and both combined are now described in order to investigate the radiative impact of the WV changes relative to those from the dust.

Figure 4 shows the shortwave DRE as a function of AOD for each experiment at the TOA, surface and for the atmospheric column. DREs are relative to the CONTROL experiment, where WV is derived from conditions where AOD<0.3. The results show that in the shortwave spectrum, the main driver of the DRE is always dust, since the WV DREs are comparatively small. Increased dust AOD leads to a more negative TOA DRE, a more negative surface DRE, and larger atmospheric heating.

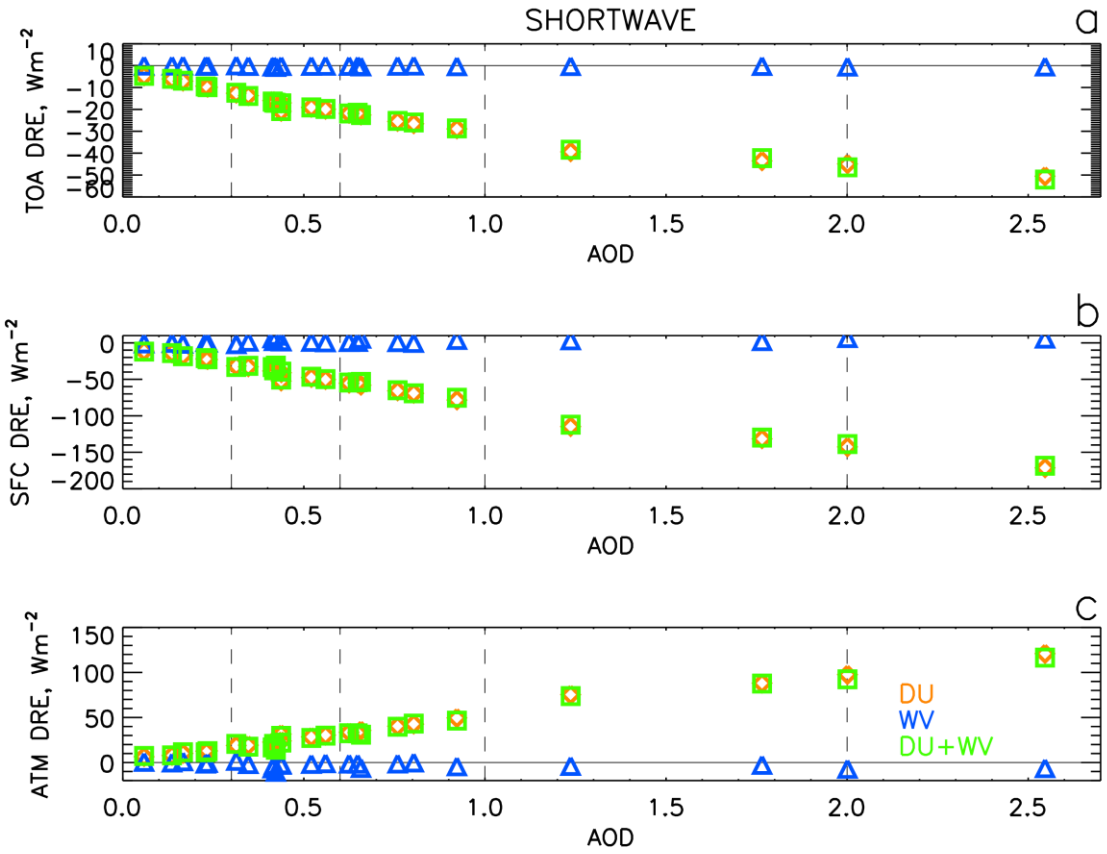

Figure 4. Shortwave DRE relative to control experiment for the inclusion of dust only (DU, orange), WV only (blue) and dust and WV (DU+WV, green), as a function of 550 nm AOD. Panels show (a) DRE at the TOA, (b) surface and (c) atmospheric column. Vertical dashed lines indicate AOD categories.

Figure 5 shows DREs as a function of AOD, but for the longwave spectrum. Here, the WV DRE exerts a large enough effect to alter the DRE significantly. At the TOA dust generates a positive LW DRE (orange points), which increases with AOD. (The exception are the two 'dust front' cases with the highest AOD, where the dust was lower in the atmosphere resulting in weaker LW DREs). The WV TOA DRE is also mostly positive and also increases with AOD (blue data points). This is consistent with increased WV, as observed in the upper-SAL, and will be investigated further in Section 3.3. As a result of the positive DRE due to WV, the DU+WV LW TOA DRE (green data points) is significantly larger than due to dust only, with values increasing by an average of 30% and a wide range of -27% to 292%.

At the surface and through the atmospheric column, dust causes a surface warming and an atmospheric cooling. The WV DRE is the opposite, resulting in a negative surface DRE and atmospheric heating. This is consistent with a net reduction in WV, and Section 3.3 will demonstrate that these changes are driven by a reduction in lower-SAL WV. At the surface, this results in a reduced LW DRE from DU+WV compared to DU alone, with values reducing by 52% on average. In the atmosphere, WV changes the sign of atmospheric heating, from a mean of -1.5 Wm^{-2} for DU to 5.5 Wm^{-2} for DU+WV. This could influence SAL dynamics at nighttime when shortwave influences are inactive.

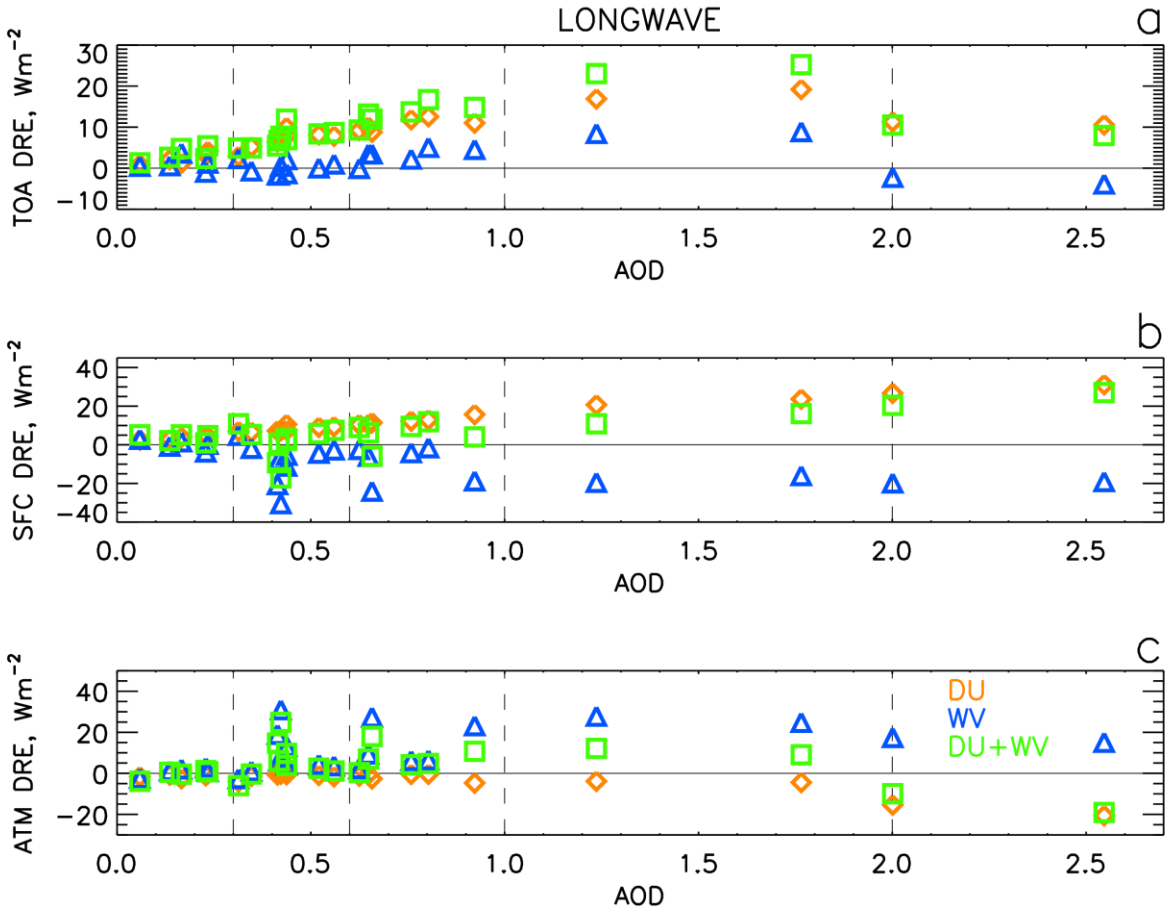

Figure 5. Longwave DRE relative to control experiment for the inclusion of dust only (DU, orange), WV only (blue) and dust and WV (DU+WV, green), as a function of 550 nm AOD. Panels show (a) DRE at the TOA, (b) surface and (c) atmospheric column. Vertical dashed lines indicate AOD categories.

Figure 6 shows the total (SW+LW) DREs as a function of AOD, and demonstrates how the dust and WV shortwave and longwave impacts from Figures 4 and 5 combine. The total TOA DRE for dust is negative, reflecting the larger magnitude originating from the SW dust DRE compared to the LW. WV TOA DREs are positive, driven by the LW DRE from WV. The net effect of including the observed WV profiles is to reduce the total negative DRE for DU+WV compared to DU alone. Overall including WV effects (excluding the dust front case) increases the TOA DRE from dust by -1.5 to 7.3 Wm^{-2} (mean of 1.3 Wm^{-2}) or increases the negative DRE by -17 to 64% (mean of 11%).

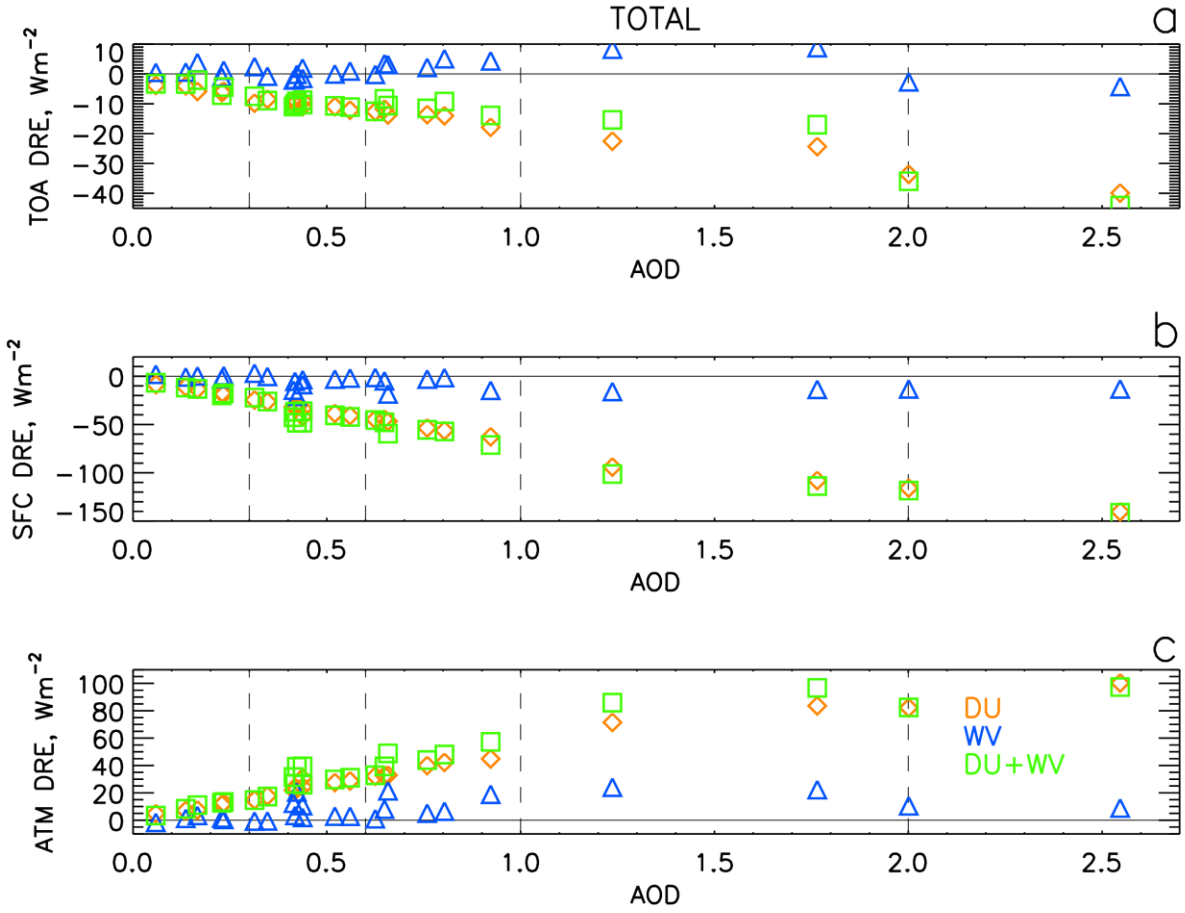

Figure 6. Total (shortwave plus longwave) DRE relative to control experiment for the inclusion of dust only (DU, orange), WV only (blue) and dust and WV (DU+WV, green), as a function of 550 nm AOD. Panels show (a) DRE at the TOA, (b) surface and (c) atmospheric column. Vertical dashed lines indicate AOD categories.

Figure 6 shows that at the surface, the main driver of the total DRE is dust, where the large negative SW DREs are slightly reduced in magnitude by positive values from the LW spectrum. WV DREs at the surface are small and negative and reduce the SFC DRE by a mean of 8% for DU+WV compared to DU. In the atmospheric column, dust is also the main driver of atmospheric heating, originating from large positive SW values shown in Figure 3. However, here the WV change can act to enhance this heating from -1 to 16 Wm^{-2} (mean of 5 Wm^{-2} or 17%), as a result of the LW WV effect.

3.3 Impact of WV in the lower and upper-SAL

Figure 7 and Figure 8 show the LW DREs as a function of PWV in the lower-SAL and upper-SAL respectively, to isolate the impacts of the changed WV structure with increasing dust, whereby WV in the upper-SAL increases, but decreases in the lower-SAL.

In Figure 7, clear relationships between PWV_lower and both surface and atmospheric LW DRE can be seen for water vapor (blue data points). In the atmosphere (panel c), a drier lower-SAL results in relatively more atmospheric heating (or equivalently less atmospheric cooling), while

at the surface, drier lower-SAL conditions result in a more negative LW DRE because less radiation is emitted downwards by the drier atmosphere.

Under dustier conditions when the lower-SAL is drier, the DU experiment mostly results in slightly negative ATM DRE values (atmospheric cooling, orange points in Figure 7c). The addition of the WV DRE changes are large enough to change the sign of ATM DRE and result in atmospheric heating for DU+WV (green points). Thus the change in sign from cooling due to heating (also seen in Figure 5c) for DU+WV compared to DU is explained by lower moisture content in the lower-SAL, and the LW ATM DRE for WV increases as moisture in the lower-SAL decreases. In Figure 6b, a drier, dustier lower-SAL results in a positive surface DRE for DU. Since the WV surface DRE is negative, values for DU+WV are sometimes large enough to change the sign compared to DU. In contrast the TOA DRE shows no dependence on WV in the lower SAL in Figure 6a.

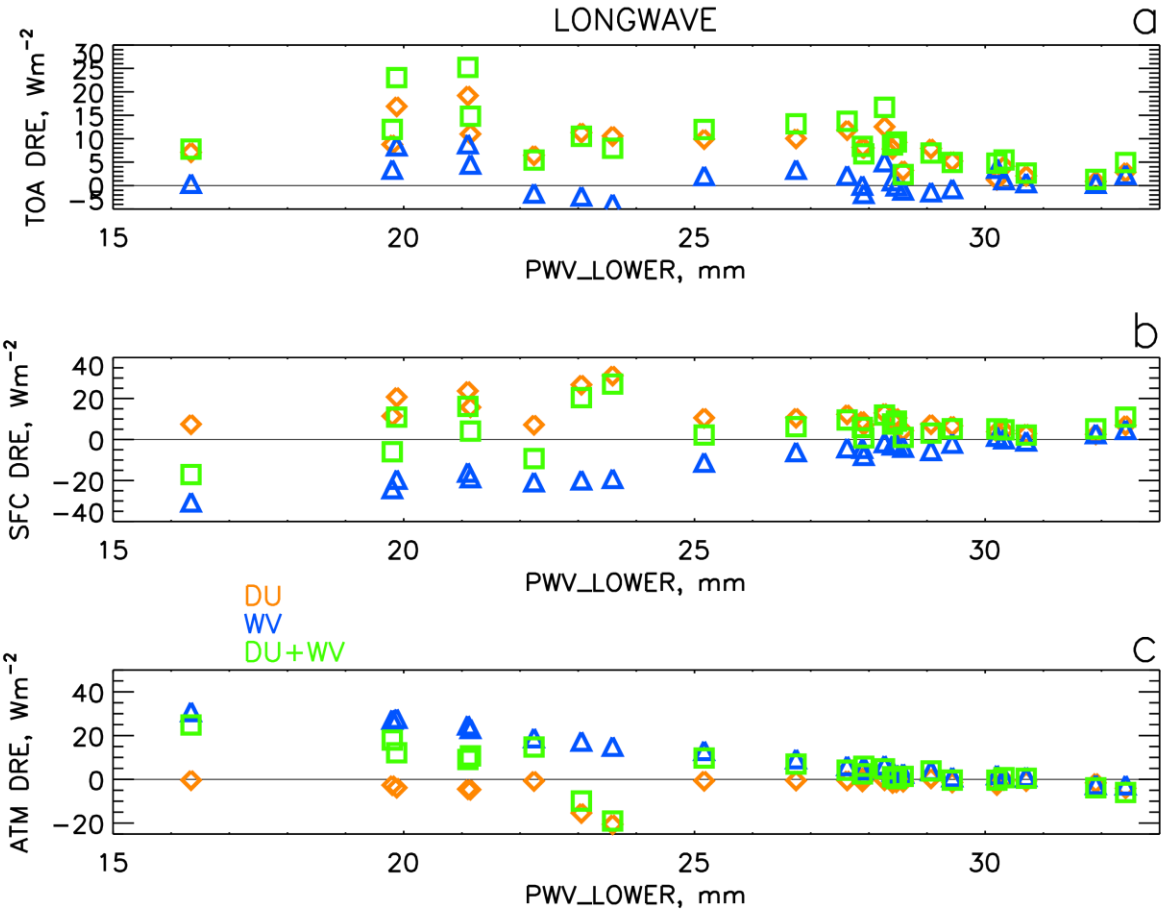

Figure 7. Longwave DRE relative to control experiment, as a function of the lower SAL PWV (PWV_lower), for the inclusion of dust only (DU, orange), WV only (blue) and dust and WV (DU+WV, green). Panels show (a) DRE at the TOA, (b) surface and (c) atmospheric column.

Figure 8 shows the DREs as a function of PWV in the upper-SAL. Although PWV_upper has no observable effect over the LW DRE at the surface and on the total atmospheric column, it has a strong effect on the LW DRE at the TOA. Larger PWV_upper (associated with increased

dustiness) results in larger, more positive LW TOA DREs due to reduced outgoing longwave radiation. This is seen for both the WV and DU experiments. When WV in the upper-SAL is higher, its proximity to the TOA (compared to the lower SAL) means that enhanced upper-SAL WV results in less LW radiation being emitted and therefore a warming effect results. At the same time, since dust AOD and PWV_upper are related, the LW dust TOA DRE also increases for high PWV_upper values. As a result, the two effects act in the same direction and increase the DU+WV TOA DRE.

This also explains the trend seen in Figure 5a, and confirms that the TOA WV effect is controlled by changes to PWV_upper, rather than PWV_lower. Thus increases in dust and increased PWV_upper both act to cause and amplify a positive LW TOA DRE.

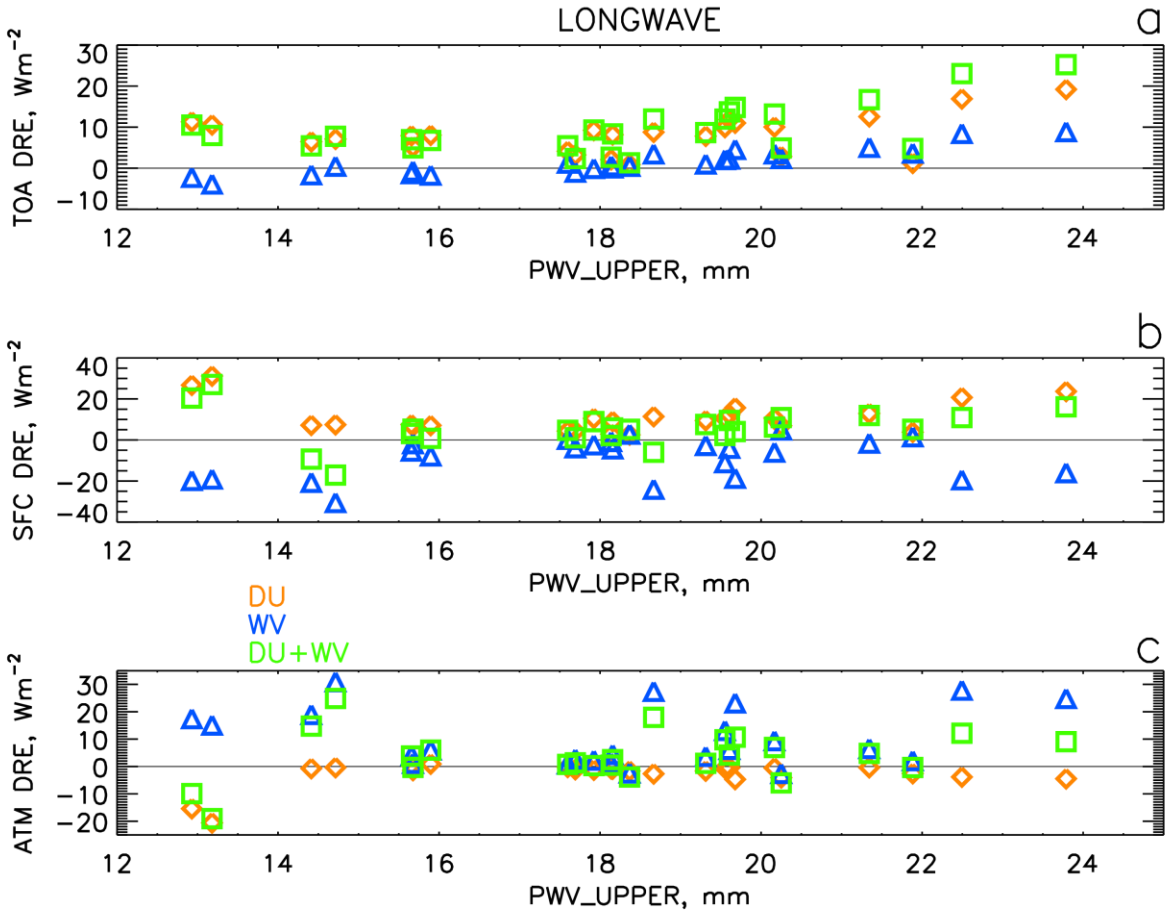

Figure 8. Longwave DRE relative to control experiment, as a function of the upper SAL PWV (PWV_upper), for the inclusion of dust only (DU, orange), WV only (blue) and dust and WV (DU+WV, green). Panels show (a) DRE at the TOA, (b) surface and (c) atmospheric column.

Figure 9 shows the absolute heating rates for the control and changes in heating rates for each experiment for the SW, LW and total relative to the control. It can be seen that dust (Figure 9 d-f) causes a SW heating, a LW cooling, and an total heating. In the SW, WV (Figure 9g) causes a slight heating at higher altitudes which is stronger and higher for larger AOD where PWV_upper is larger. In the LW (panel h), the impact of increased PWV_upper and decreased PWV_lower

443 can be seen. When AODs are higher, more upper-SAL cooling from enhanced moisture and less
444 mid-SAL cooling (i.e. warming) from enhanced dryness is observed. This results in changes to
445 total heating rates of up to -2.5 K/d in the upper SAL and +1.5 K/d through the lower-SAL due
446 to the dust-related WV changes (panel i).
447
448 Comparing Fig f to Fig l shows the changes in total heating rates due to DU+WV compared to
449 dust alone. We see that the total WV+DU heating rates (fig l) show extra cooling at heights
450 above 550 hPa and increased heating through the mid-SAL (~950 to 600 hPa), higher by about 2
451 K/d relative to Fig f . Although increased dust was associated with decreased PWV_lower at
452 heights beneath 820 hPa, the radiative heating effects of this WV change are felt throughout the
453 wider column up to around 680 hPa. As a result, the PWV_lower changes control the ATM
454 DRE, determining atmospheric heating or cooling, as shown in Figure 6c. It is also notable that
455 only by including the enhanced WV in the upper SAL, is the cold anomaly in potential
456 temperatures seen in Figure 3d consistent with the additional cooling rates above around 500
457 hPa.
458

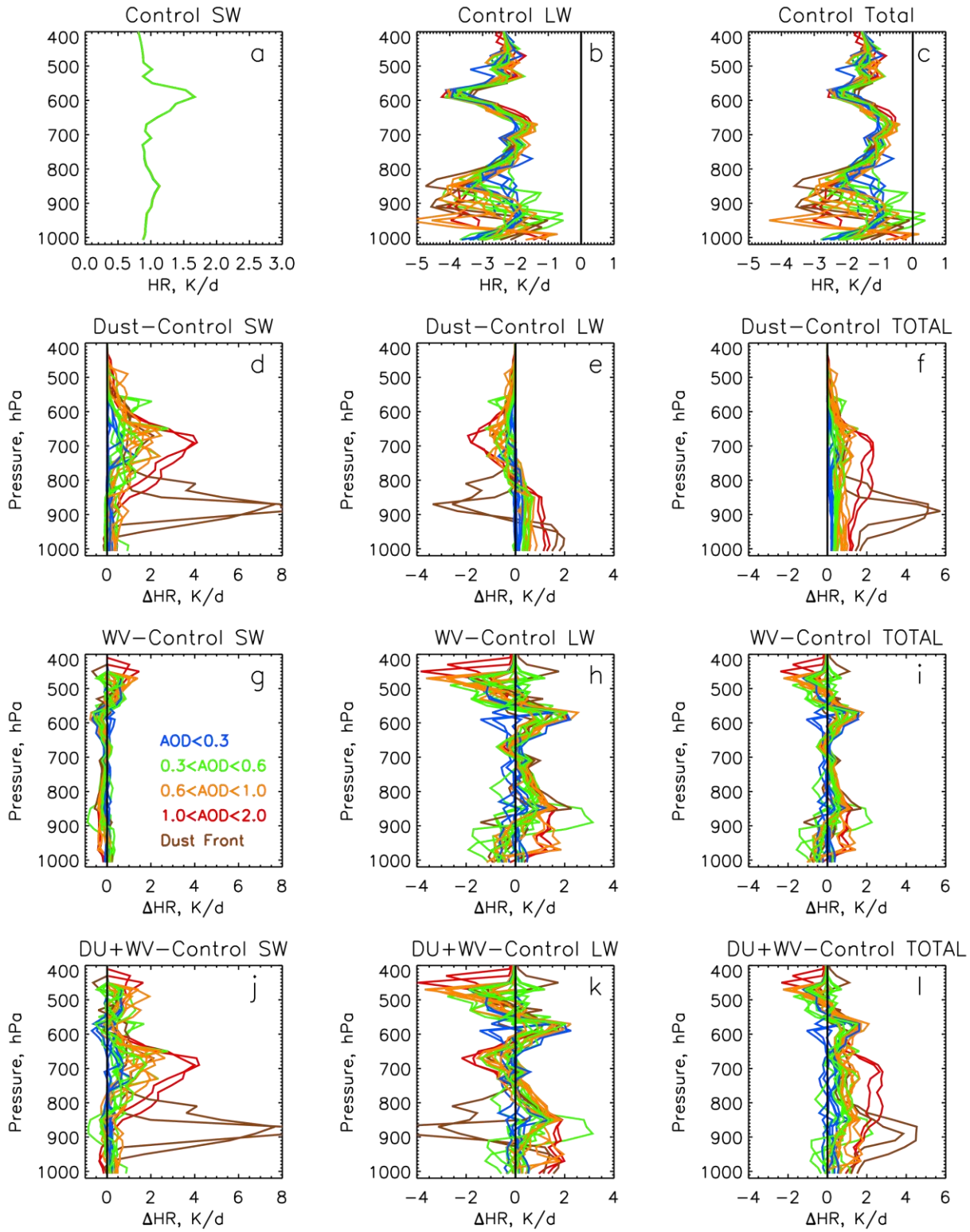

Figure 9. Top row: absolute heating rates for the CONTROL for all profiles for (a) SW, (b) LW, (c) total (SW+LW). Other rows: changes in heating rates (HR, K/day) between each experiment and the control, for (d-f) DU, (g-i) WV (middle row) and (j-l) WV+DU (bottom row), for the SW

463 spectrum (left), LW spectrum (center) and total (SW plus LW, right). Profiles are colored as a
464 function of AOD.

465 **4 Discussion**

466 This work finds elevated moisture levels in the upper SAL associated with dust, and
467 demonstrates that this increased moisture is important in determining the magnitude, and
468 potentially the sign of the radiative effect exerted by the dusty SAL. The elevated moisture found
469 in the upper SAL differs to the frequently reported SAL characteristics of it being a
470 straightforward dry layer, suggesting that more complexity and vertical detail is required to
471 accurately reflect the SAL and its radiative impacts.
472
473 Much previous work characterizing the SAL focuses on the its lower atmospheric structure,
474 particularly heating rates at around 850 hPa and their relation to sustaining the temperature
475 inversion between the marine boundary layer and the SAL base, due to its importance in
476 suppression of convection and potentially impeding tropical cyclone development (e.g. Dunion
477 and Velden (2004); Wong et al. (2009)). However, a few studies have focused more on the
478 structure of the entire depth of the SAL. For example, Braun (2010) find a 400-600hPa
479 moistening across Africa to Saudi Arabia relative to the very dry Saharan air below, due to deep,
480 dry convective mixing over the Sahara. This structure has sometimes been found at the west
481 coast of Africa and also downstream. Ismail et al. (2010) show a case where WV mixing ratios
482 were around 2 to 7 g/kg throughout the SAL. They attribute this increased moisture to
483 midaltitude convection as a result of intensification of an AEW, pointing out that increased WV
484 leaves the SAL more amenable to convection. Thus the elevated WV in the upper SAL may have
485 a wider dynamical impact than has been possible to examine here.
486
487 Despite the fact that the observations presented here show enhanced moisture in the upper-SAL
488 compared to background conditions, we do not suggest that the SAL is not a well-mixed,
489 elevated layer. This is illustrated through the schematic shown in Figure 10, which is based on
490 the observations shown in Figure 3. The background (non-SAL) profiles of potential temperature
491 and water vapor mixing ratio are represented by gradually increasing and decreasing values,
492 respectively. Therefore, when a well-mixed layer (the SAL), with near-constant potential
493 temperature and water vapor mixing ratio, is imposed, this results in either a positive or negative
494 anomaly in both its upper and lower portions. Therefore, the results presented in this work do not
495 oppose the previous documentation of the SAL evidencing its well-mixed nature, they simply
496 expose the extension of the well-mixed SAL upwards which results in the cooler, moister
497 anomalies shown in Figure 10. The absolute magnitude of water vapor mixing ratios in the SAL
498 will determine the magnitude of the anomalies relative to the background condition, such that a
499 moister, well-mixed SAL will shift the line of constant q shown in Figure 10 to the right,
500 increasing the moist anomaly.
501

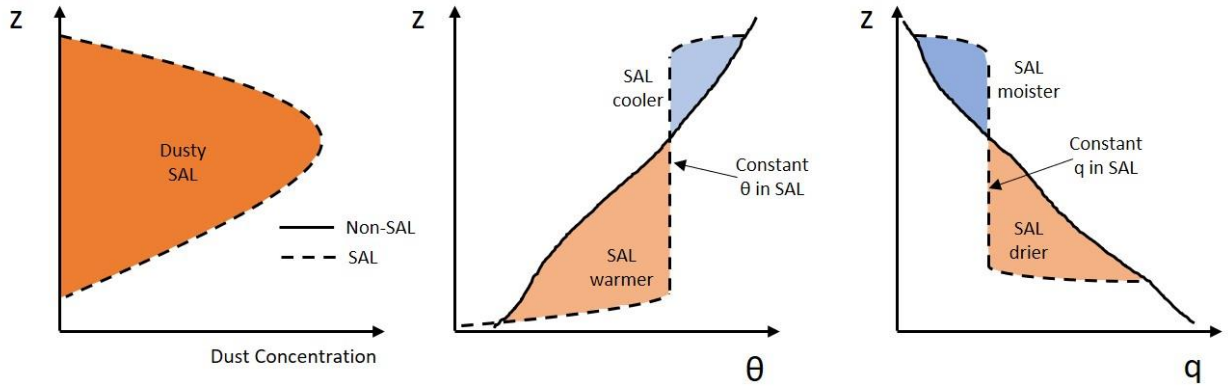

Figure 10: Schematic depicting anomalies observed in the dusty SAL. SAL conditions are characterized by well-mixed, elevated potential temperature (θ) and water vapor mixing ratios (q). Compared to the background, non-SAL environment, this results in a warmer, drier lower-SAL and a cooler, moister upper-SAL.

Gutleben et al. (2019) present airborne observations from a case study in the western Atlantic SAL. Although they find that WV mixing ratios increased in the SAL relative to the free troposphere, their figures show that the SAL was actually drier than the tropical standard atmosphere. Nevertheless, their results show that the increase from dry to moist air descending into the top of the SAL was important for driving strong LW cooling rates at the top of the SAL, similar to the heating rate profiles shown here.

Adebiyi et al. (2015) present similar findings to this work, but for biomass burning aerosol (BBA) layers over the southeast Atlantic containing enhanced moisture. They find that this anomalous moisture leads to anomalous LW cooling in the layer counteracting the SW heating from the BBA. However, due to the negligible LW radiative effect of BBA, the LW and SW radiative effects of WV combine differently in the results of Adebiyi et al. (2015) to those presented here. Clearly dust layers are not the only type of aerosol layer which can be collocated with enhanced WV, and there may be more instances of transported aerosol layers globally where WV changes exert an effect.

As well as influencing the radiative effect, enhanced upper SAL moisture and associated cooling at these altitudes may also influence mid-level altocumulus cloud development. For example, it could be important to the development of the frequently observed altocumulus cloud capping the SABL and SAL, as shown in Kealy et al. (2017) and Mantsis et al. (2020), which play an important radiative role.

The additional cooling at the top of the SAL due to WV may help to maintain its well-mixed vertical structure, aiding subsidence at the SAL top, combined with ascent at the SAL base due to the well-known lower SAL heating from both dust and water vapor. This is consistent with a lowering of the SAL top towards the west, and a rising of the SAL base (e.g. Liu et al. (2008), Tsamalis et al. (2013)).

An interesting question regarding elevated moisture in the upper SAL is whether this is a feature that has simply been under-investigated in the past, or whether the moistening is a temporal

trend. Evan et al. (2015) show that WV content in the Saharan heat low region over Africa has increased over the last 30 years as a result of a WV-temperature feedback cycle. Thus it seems plausible that the SAL, outflowing from the Sahara, may be moistening as a consequence. Cold pool outflows (haboobs) play a key role in the transport of both water vapor and dust into the Saharan heat low region (Allen et al., 2013; Engelstaedter et al., 2015; Flamant et al., 2007; Marsham et al., 2013; Yu et al., submitted) where it is mixed throughout the deep Saharan boundary layer with dust, before being transported westwards as the SAL. Therefore another question which arises is whether the intensity and/or frequency of cold pool outflows over west Africa has changed over time.

The ability of enhanced moisture in the upper-SAL to reduce the magnitude of the negative TOA radiative effect of the SAL, shifting it towards positive values, is particularly important when considered with other recent developments in the literature. Adebiyi and Kok (2020) have shown that climate models miss most coarse dust in the atmosphere, and including this missed coarse dust adds a TOA radiative warming effect of 0.15 Wm^{-2} globally. Di Biagio et al. (2020) show that updated dust optical properties and inclusion of dust sizes larger than 20 µm further shifts the global direct radiative effect of dust away from a cooling effect, to -0.03 Wm^{-2}. When combined with potential increases in upper SAL moisture, this will further shift the regional radiative effect of dust towards a net warming effect over the tropical Atlantic. The importance of these combined effects will be further increased in regions where dust emissions are increasing over time, exerting a radiative forcing which may tend towards positive values.

Another pertinent question concerns potential mechanisms which may enable coarse dust particles to be transported further than expected (Mallios et al., 2020; O'Sullivan et al., 2020; Ryder et al., 2019; van der Does et al., 2018; Weinzierl et al., 2017). This work shows that as well as a significant day-time shortwave atmospheric column heating from dust, the reduced lower-SAL moisture which occurs under dustier conditions can lead to increased atmospheric longwave heating throughout most of the SAL depth, which would dominate at night. Both these mechanisms may contribute to upward dynamic effects which may increase the lifetime and long-range transport of dust particles, including the coarser sizes.

Finally there are several uncertainties and limitations inherent in this work. Firstly, the observations, although constituting 24 profiles over the course of 19 days and 5 dust events, are only representative of August 2015 and the eastern Tropical Atlantic, and a wider spatial and temporal analysis would be beneficial. For example, questions such as whether the upper-SAL WV enhancement is present throughout the summer dust season, and how this may vary year to year and westwards across the Atlantic are important.

The main uncertainty in this work stems from the optical properties of the dust applied in the RTM, which were setup specifically to match the in-situ size and composition results measured during the AER-D campaign (Ryder et al., 2018). As a sensitivity study, optical properties were also selected to represent more extreme values of absorbing dust and less absorbing dust. The impact of the WV perturbation to the DRE is quite sensitive to the optical properties assumed. For example, at the TOA, the total DRE due to dust approaches zero when dust is very absorbing in the SW. Therefore, when the WV changes are also included, which are positive, the final TOA DRE from DU+WV can sometimes change sign, becoming positive. Conversely, for less

absorbing dust with a high SSA, the dust DRE at the TOA is more negative. Therefore, proportionally the addition of a positive WV DRE results in a smaller fractional decrease in the negative DRE. Nevertheless, whatever the chosen optical properties of dust are, the radiative changes due to the WV profile remain important.

Finally, this work does not account for any changes in humidity upon the microphysical properties of the dust, such as possible hydrophilic growth and changes in scattering properties. Although it is possible that hydrophobic dust particles become more hydrophilic during transport through chemical coatings such as sulfate, there is much uncertainty in understanding of this process and some studies show that this is not an important factor during trans-Atlantic dust transport (Denjean et al., 2015). Additionally, measurements of scattering and absorption at different humidities were not taken during AER-D.

5 Conclusions

This work presents results from 24 in-situ aircraft profiles from 5 dust events over the eastern tropical Atlantic during August 2015. It has been shown that as dust loadings increase and the thermal characteristics of the SAL develop, WV mixing ratios decrease in the lower-SAL (p>820 hPa) and increase in the upper SAL (480 hPa to 780 hPa) at a mean rate of 3.8 mm per unit AOD.

Conventionally the SAL is considered to be a warm, dry, elevated, well-mixed layer which is frequently dusty (e.g. Carlson and Prospero (1972)). Therefore the observations of enhanced moisture in the upper SAL under dusty conditions are somewhat contradictory to this description. This can be reconciled by observations presented here showing that the SAL has well-mixed characteristics, but by extending them in altitude where the SAL then becomes cooler and moister than the background conditions.

The radiative impact of the observed WV and dusty profiles has been quantified using a radiative transfer model. The enhanced upper-SAL moisture was found to have most effect at the TOA, causing a positive DRE, counteracting the negative TOA DRE exerted by the dust. When both WV and dust were included, the negative DRE at the TOA from dust was reduced in magnitude by up to 64% with a mean of 11%. Thus, accounting for the complex WV profile is crucial in determining the radiative effect of the dusty SAL, and is significantly different to simply assuming a dry profile.

The total DRE at the surface and in the atmosphere were dominated by dust effects, but were enhanced by WV reductions in the lower-SAL. Decreases in lower-SAL WV acted to increase the negative surface DRE from dust by 8% and increase atmospheric heating by 17% on average.

Changes in in the total DRE were driven by WV changes from the longwave spectrum. Less WV in the lower-SAL under dusty conditions resulted in a more negative surface LW DRE due to less emission of LW radiation from WV towards the surface from the lower-SAL. At the same time, less LW cooling occurred in the drier lower-SAL due to smaller LW absorption. In the LW spectrum, the inclusion of the dry lower-SAL results in change in sign from net cooling to net

heating compared to dust only, and could be important for nighttime dynamics and dust transport within the SAL.

Heating rate profile changes due to WV and dust in the SAL were calculated. Dust was found to cause a net heating, driven by SW heating, whereas the WV structure generated cooling in the upper-SAL and heating throughout the mid to lower-SAL compared to background conditions, amplifying the heating occurring here due to dust. The upper-SAL cooling under dustier conditions due to WV is consistent with colder upper SAL temperatures in dusty conditions.

Although this work only represents dust events in the SAL from August 2015, increased moisture in the SAL is consistent with an observed moistening of the Saharan heat low region over west Africa over the last 30 years as part of a feedback cycle driven by increased temperatures (Evan et al., 2015). Cold pool outflows play a crucial role in transporting WV into the Saharan heat low region (Allen et al., 2013; Engelstaedter et al., 2015; Flamant et al., 2007; Marsham et al., 2013). Therefore future work should evaluate the prevalence of moisture on wider temporal and spatial scales than has been possible here, and also examine whether there are temporal trends in the transport of WV and dust northwards into the Sahara by cold pool outflows, potentially as a result of climate change, as well as examining the ability of models with explicit dust schemes to reproduce the dust-WV relationship shown here.

Acknowledgments

C.L.Ryder received funding from NERC Independent Research Fellowship NE/M018288/1. Airborne data from the BAe 146 were obtained using the BAe 146-301 Atmospheric Research Aircraft operated by Directflight Ltd and managed by FAAM, which was a joint entity of the NERC and the UK Met Office. Keith Shine, Ross Herbert and Franco Marenco are thanked for useful discussions relating to this work.

Data

Aircraft data is available at the Centre for Environmental Data Archive at: http://catalogue.ceda.ac.uk/uuid/d7e02c75191a4515a28a208c8a069e70

References

Adebiyi, A. A., & Kok, J. F. (2020). Climate models miss most of the coarse dust in the atmosphere. *Science Advances, 6*(15). doi:10.1126/sciadv.aaz9507

Adebiyi, A. A., Zuidema, P., & Abel, S. J. (2015). The Convolution of Dynamics and Moisture with the Presence of Shortwave Absorbing Aerosols over the Southeast Atlantic. *Journal of Climate, 28*(5), 1997-2024. doi:10.1175/Jcli-D-14-00352.1

Allen, C. J. T., Washington, R., & Engelstaedter, S. (2013). Dust emission and transport mechanisms in the central Sahara: Fennec ground-based observations from Bordj Badji Mokhtar, June 2011. *Journal of Geophysical Research-Atmospheres, 118*(12), 6212-6232. doi:10.1002/jgrd.50534

Anderson, G. P., Clough, S. A., Kneizys, F. X., Chetwynd, J. H., & Shettle, E. P. (1986). *AFGL atmospheric constituent profiles (0-120 km), Technical Report AFGL-TR-86-0110, AFGL (OPI), Hanscom.* (AFB, MA. 01736). Retrieved from

Balkanski, Y., Schulz, M., Claquin, T., & Guibert, S. (2007). Reevaluation of Mineral aerosol radiative forcings suggests a better agreement with satellite and AERONET data. *Atmospheric Chemistry and Physics, 7*, 81-95.

Braun, S. A. (2010). Reevaluating the Role of the Saharan Air Layer in Atlantic Tropical Cyclogenesis and Evolution. *Monthly Weather Review, 138*(6), 2007-2037. doi:10.1175/2009mwr3135.1

Carlson, T. N. (2016). The Saharan Elevated Mixed Layer and its Aerosol Optical Depth. *The Open Atmospheric Science Journal, 10*, 26-38. doi:DOI: 10.2174/1874282301610010026

Carlson, T. N., & Benjamin, S. G. (1980). Radiative Heating Rates for Saharan Dust. *Journal of the Atmospheric Sciences, 37*(1), 193-213. doi:Doi 10.1175/1520-0469(1980)037<0193:Rhrfsd>2.0.Co;2

Carlson, T. N., & Prospero, J. (1972). The Large-Scale Movement of Saharan Air Outbreaks over the Northern Equatorial Atlantic. *Journal of Applied Meteorology and Climatology, 11*(2), 283-297. doi:https://doi.org/10.1175/1520-0450(1972)011<0283:TLSMOS>2.0.CO;2

Colarco, P. R., Nowottnick, E. P., Randles, C. A., Yi, B. Q., Yang, P., Kim, K. M., . . . Bardeen, C. G. (2014). Impact of radiatively interactive dust aerosols in the NASA GEOS-5 climate model: Sensitivity to dust particle shape and refractive index. *Journal of Geophysical Research-Atmospheres, 119*(2), 753-786. doi:10.1002/2013jd020046

Cusack, S., Edwards, J. M., & Crowther, J. M. (1999). Investigating k distribution methods for parameterizing gaseous absorption in the Hadley Centre Climate Model. *Journal of Geophysical Research-Atmospheres, 104*(D2), 2051-2057. doi:Doi 10.1029/1998jd200063

Denjean, C., Caquineau, S., Desboeufs, K., Laurent, B., Maille, M., Rosado, M. Q., . . . Formenti, P. (2015). Long-range transport across the Atlantic in summertime does not enhance the hygroscopicity of African mineral dust. *Geophysical Research Letters, 42*(18), 7835-7843. doi:10.1002/2015gl065693

Di Biagio, C., Balkanski, Y., Albani, S., Boucher, O., & Formenti, P. (2020). Direct Radiative Effect by Mineral Dust Aerosols Constrained by New Microphysical and Spectral Optical Data. *Geophysical Research Letters, 47*(2). doi:10.1029/2019GL086186

Doherty, O. M., & Evan, A. T. (2014). Identification of a new dust-stratocumulus indirect effect over the tropical North Atlantic. *Geophysical Research Letters, 41*(19), 6935-6942. doi:10.1002/2014gl060897

Dubovik, O., Holben, B., Eck, T. F., Smirnov, A., Kaufman, Y. J., King, M. D., . . . Slutsker, I. (2002). Variability of absorption and optical properties of key aerosol types observed in worldwide locations. *Journal of the Atmospheric Sciences, 59*(3), 590-608. doi:Doi 10.1175/1520-0469(2002)059<0590:Voaaop>2.0.Co;2

Dunion, J. P. (2011). Rewriting the Climatology of the Tropical North Atlantic and Caribbean Sea Atmosphere. *Journal of Climate, 24*(3), 893-908. doi:10.1175/2010jcli3496.1

Dunion, J. P., & Velden, C. S. (2004). The impact of the Saharan air layer on Atlantic tropical cyclone activity. *Bulletin of the American Meteorological Society, 85*(3), 353-+. doi:Doi 10.1175/Bams-85-3-353

Edwards, J. M., & Slingo, A. (1996). Studies with a flexible new radiation code .1. Choosing a configuration for a large-scale model. *Quarterly Journal of the Royal Meteorological Society, 122*(531), 689-719.

Engelstaedter, S., Washington, R., Flamant, C., Parker, D. J., Allen, C. J. T., & Todd, M. C. (2015). The Saharan heat low and moisture transport pathways in the central Sahara-Multiaircraft observations and Africa-LAM evaluation. *Journal of Geophysical Research-Atmospheres, 120*(10), 4417-4442. doi:10.1002/2015jd023123

Evan, A. T., Flamant, C., Lavaysse, C., Kocha, C., & Saci, A. (2015). Water Vapor-Forced Greenhouse Warming over the Sahara Desert and the Recent Recovery from the Sahelian Drought. *Journal of Climate, 28*(1), 108-123. doi:10.1175/Jcli-D-14-00039.1

Flamant, C., Chaboureau, J. P., Parker, D. J., Taylor, C. A., Cammas, J. P., Bock, O., . . . Pelon, J. (2007). Airborne observations of the impact of a convective system on the planetary boundary layer thermodynamics and aerosol distribution in the inter-tropical discontinuity region of the West African Monsoon. *Quarterly Journal of the Royal Meteorological Society, 133*(626), 1175-1189. doi:Doi 10.1002/Qj.97

Gutleben, M., Gross, S., Wirth, M., Emde, C., & Mayer, B. (2019). Impacts of Water Vapor on Saharan Air Layer Radiative Heating. *Geophysical Research Letters, 46*(24), 14854-14862. doi:10.1029/2019gl085344

Hess, M., Koepke, P., & Schult, I. (1998). Optical properties of aerosols and clouds: The software package OPAC. *Bulletin of the American Meteorological Society, 79*(5), 831-844. doi:Doi 10.1175/1520-0477(1998)079<0831:Opoaac>2.0.Co;2

Ismail, S., Ferrare, R. A., Browell, E. V., Kooi, S. A., Dunion, J. P., Heymsfield, G., . . . Anderson, B. (2010). LASE Measurements of Water Vapor, Aerosol, and Cloud Distributions in Saharan Air Layers and Tropical Disturbances. *Journal of the Atmospheric Sciences, 67*(4), 1026-1047. doi:10.1175/2009jas3136.1

Kanitz, T., Engelmann, R., Heinold, B., Baars, H., Skupin, A., & Ansmann, A. (2014). Tracking the Saharan Air Layer with shipborne lidar across the tropical Atlantic. *Geophysical Research Letters, 41*(3), 1044-1050. doi:10.1002/2013gl058780

Karyampudi, V. M., Palm, S. P., Reagen, J. A., Fang, H., Grant, W. B., Hoff, R. M., . . . Melfi, S. H. (1999). Validation of the Saharan dust plume conceptual model using lidar, Meteosat, and ECMWF data. *Bulletin of the American Meteorological Society, 80*(6), 1045-1075.

Kealy, J. C., Marenco, F., Marsham, J. H., Garcia-Carreras, L., Francis, P. N., Cooke, M. C., & Hocking, J. (2017). Clouds over the summertime Sahara: an evaluation of Met Office retrievals from Meteosat Second Generation using airborne remote sensing. *Atmospheric Chemistry and Physics, 17*(9), 5789-5807. doi:10.5194/acp-17-5789-2017

Korolev, A. V., Strapp, J. W., Isaac, G. A., & Nevzorov, A. N. (1998). The Nevzorov airborne hot-wire LWC-TWC probe: Principle of operation and performance characteristics. *Journal of Atmospheric and Oceanic Technology, 15*(6), 1495-1510. doi:Doi 10.1175/1520-0426(1998)015<1495:Tnahwl>2.0.Co;2

Liu, D. T., Taylor, J., Crosier, J., Marsden, N., Bower, K. N., Lloyd, G., . . . Choularton, T. W. (2018). Aircraft and ground measurements of dust aerosols over the west African coast in summer 2015 during ICE-D and AER-D. *Atmospheric Chemistry and Physics, 18*(5), 3817-3838. doi:10.5194/acp-18-3817-2018

Liu, Z. Y., Omar, A., Vaughan, M., Hair, J., Kittaka, C., Hu, Y. X., . . . Pierce, R. (2008). CALIPSO lidar observations of the optical properties of Saharan dust: A case study of long-range transport. *Journal of Geophysical Research-Atmospheres, 113*(D7). doi:Doi 10.1029/2007jd008878

759 Mallios, S. A., Drakaki, E., & Amiridis, V. (2020). Effects of dust particle sphericity and
760 orientation on their gravitational settling in the earth's atmosphere. *Journal of Aerosol*
761 *Science, 150*. doi:10.1016/j.jaerosci.2020.105634
762 Manners, J., Edwards, J., Hill, P., & Thelen, J.-C. (2017). *SOCRATES Technical Guide Suite Of*
763 *Community RAdiative Transfer codes based on Edwards and Slingo*. Retrieved from
764 Exeter:
765 Mantsis, D. F., Sherwood, S., Dixit, V., Morrison, H., & Thompson, G. (2020). Mid-level clouds
766 over the Sahara in a convection-permitting regional model. *Climate Dynamics, 54*(7-8),
767 3425-3439. doi:10.1007/s00382-020-05188-4
768 Marenco, F., Ryder, C., Estelles, V., O'Sullivan, D., Brooke, J., Orgill, L., . . . Gallagher, M.
769 (2018). Unexpected vertical structure of the Saharan Air Layer and giant dust particles
770 during AER-D. *Atmospheric Chemistry and Physics, 18*(23), 17655-17668.
771 doi:10.5194/acp-18-17655-2018
772 Marsham, J. H., Hobby, M., Allen, C. J. T., Banks, J. R., Bart, M., Brooks, B. J., . . .
773 Washington, R. (2013). Meteorology and dust in the central Sahara: Observations from
774 Fennec supersite-1 during the June 2011 Intensive Observation Period. *Journal of*
775 *Geophysical Research-Atmospheres, 118*(10), 4069-4089. doi:10.1002/jgrd.50211
776 Marsham, J. H., Parker, D. J., Grams, C. M., Taylor, C. M., & Haywood, J. M. (2008). Uplift of
777 Saharan dust south of the intertropical discontinuity. *Journal of Geophysical Research-*
778 *Atmospheres, 113*(D21). doi:Doi 10.1029/2008jd009844
779 Marsham, J. H., Parker, D. J., Todd, M. C., Banks, J. R., Brindley, H. E., Garcia-Carreras, L., . . .
780 Ryder, C. L. (2016). The contrasting roles of water and dust in controlling daily
781 variations in radiative heating of the summertime Saharan heat low. *Atmospheric*
782 *Chemistry and Physics, 16*(5), 3563-3575. doi:10.5194/acp-16-3563-2016
783 O'Sullivan, D., Marenco, F., Ryder, C. L., Pradhan, Y., Kipling, Z., Johnson, B., . . . Selmer, P.
784 (2020). Models transport Saharan dust too low in the atmosphere: a comparison of the
785 MetUM and CAMS forecasts with observations. *Atmospheric Chemistry and Physics,*
786 *20*(21), 12955-12982. doi:10.5194/acp-20-12955-2020
787 Prospero, J. M., & Carlson, T. N. (1972). Vertical and Areal Distribution of Saharan Dust over
788 Western Equatorial North-Atlantic Ocean. *Journal of Geophysical Research, 77*(27),
789 5255-&. doi:DOI 10.1029/JC077i027p05255
790 Randles, C., Kinne, S., Myhre, G., Schulz, M., Stier, P., Fischer, J., . . . Lu, P. (2012).
791 Intercomparison of shortwave radiative transfer schemes in global aerosol modeling:
792 Results from the AeroCom Radiative Transfer Experiment. *Atmos. Chem. Phys. Discuss.*,
793 *12*(12), 32631-32706. doi:doi:10.5194/acpd-12-32631-2012
794 Rothman, L. S., Barbe, A., Benner, D. C., Brown, L. R., Camy-Peyret, C., Carleer, M. R., . . .
795 Yoshino, K. (2003). The HITRAN molecular spectroscopic database: edition of 2000
796 including updates through 2001. *Journal of Quantitative Spectroscopy & Radiative*
797 *Transfer, 82*(1-4), 5-44. doi:10.1016/S0022-4073(03)00146-8
798 Ryder, C. L., Highwood, E. J., Walser, A., Seibert, P., Philipp, A., & Weinzierl, B. (2019).
799 Coarse and giant particles are ubiquitous in Saharan dust export regions and are
800 radiatively significant over the Sahara. *Atmospheric Chemistry and Physics, 19*(24),
801 15353-15376. doi:10.5194/acp-19-15353-2019
802 Ryder, C. L., Marenco, F., Brooke, J. K., Estelles, V., Cotton, R., Formenti, P., . . . Murray, B. J.
803 (2018). Coarse-mode mineral dust size distributions, composition and optical properties

804 from AER-D aircraft measurements over the tropical eastern Atlantic. *Atmospheric*
805 *Chemistry and Physics, 18*(23), 17225-17257. doi:10.5194/acp-18-17225-2018
806 Tsamalis, C., Chedin, A., Pelon, J., & Capelle, V. (2013). The seasonal vertical distribution of
807 the Saharan Air Layer and its modulation by the wind. *Atmospheric Chemistry and*
808 *Physics, 13*(22), 11235-11257. doi:10.5194/acp-13-11235-2013
809 van der Does, M., Knippertz, P., Zschenderlein, P., Harrison, R. G., & Stuut, J. B. W. (2018).
810 The mysterious long-range transport of giant mineral dust particles. *Science Advances*,
811 *4*(12). doi:10.1126/sciadv.aau2768
812 Volz, F. E. (1973). Infrared Optical-Constants of Ammonium Sulfate, Sahara Dust, Volcanic
813 Pumice, and Flyash. *Applied Optics*, *12*(3), 564-568. doi:Doi 10.1364/Ao.12.000564
814 Walters, D. N., Best, M. J., Bushell, A. C., Copsey, D., Edwards, J. M., Falloon, P. D., . . .
815 Williams, K. D. (2011). The Met Office Unified Model Global Atmosphere 3.0/3.1 and
816 JULES Global Land 3.0/3.1 configurations. *Geoscientific Model Development, 4*(4), 919-
817 941. doi:10.5194/gmd-4-919-2011
818 Weinzierl, B., Ansmann, A., Prospero, J. M., Althausen, D., Benker, N., Chouza, F., . . . Walser,
819 A. (2017). The Saharan Aerosol Long-range Transport and Aerosol-cloud-interaction
820 experiment: Overview and Selected Highlights. *Bulletin of the American Meteorological*
821 *Society, 98*(7), 1427-1451. doi:10.1175/Bams-D-15-00142.1
822 Wong, S., & Dessler, A. E. (2005). Suppression of deep convection over the tropical North
823 Atlantic by the Saharan Air Layer. *Geophysical Research Letters, 32*(9).
824 doi:10.1029/2004gl022295
825 Wong, S., Dessler, A. E., Mahowald, N. M., Yang, P., & Feng, Q. (2009). Maintenance of Lower
826 Tropospheric Temperature Inversion in the Saharan Air Layer by Dust and Dry Anomaly.
827 *Journal of Climate, 22*(19), 5149-5162. doi:10.1175/2009jcli2847.1
828 Yu, H., Tan, Q., Zhou, L., Bian, H. S., Chin, M., Ryder, C. L., . . . Holben, B. (submitted).
829 Observation and modeling of a gigantic African dust intrusion into the Caribbean Basin
830 and the southern U.S. in June 2020. *Atmos. Chem. Phys.*
831 Zdunkowski, W. G., Welch, R. M., & Korb, G. (1980). An investigation of the structure of
832 typical two-stream methods for the calculation of solar fluxes and heating rates in clouds.
833 *Beitr¨age Phys. Atmosph., 53*, 147-166.
834